Title

Deformable Joule Heating Electrode Based on Hybrid Layers of Silver Nanowires and Carbon Nanotubes and its Application in a Refreshable Multi-Cell Braille Display

Permalink

https://escholarship.org/uc/item/3pp129rv

Journal

Advanced Functional Materials, 34(33)

ISSN

1616-301X

Authors

Kim, Jinsung
Xie, Zhixin
Peng, Zihang
et al.

Publication Date

2024-08-01

DOI

10.1002/adfm.202400023

Deformable Joule heating electrode based on hybrid layers of silver nanowires and carbon nanotubes and its application in a refreshable multi-cell Braille display

Jinsung Kim, Zhixin Xie, Zihang Peng, HyeonJi Hong, Shaghayegh Shajari, Yuxuan Guo, Hanxiang Wu, Yuan Meng, Roshan Plamthottam, Yuan Zhu, Yu Qiu, Huiying Wang, Alex Cheng, and Qibing Pei*

J Kim, Z Xie, Z Peng, HJ Hong, S Shajari, Y Guo, H Wu, Y Meng, R Plamthottam, Y Zhu, Y Qiu, H Wang, A Cheng, and Q Pei
Soft Materials Research Laboratory, Department of Materials Science and Engineering
Henry Samueli School of Engineering and Applied Science
University of California
Los Angeles, 420 Westwood Plaza, Los Angeles, CA 90095, USA
E-mail: qpei@seas.ucla.edu

Abstract

Stretchable electrodes are an essential component in soft actuator systems. In particular, Joule heating electrodes (JHEs) are required for thermal actuation systems. A highly stretchable, patternable, and low-voltage operating JHE based on hybrid layers of silver nanowires (AgNWs) and carbon nanotubes (CNTs) is reported. The conductive layers were applied on a locally pre-strained bistable electroactive polymer (BSEP) membrane to form a wrinkled conductive surface with a low resistance of 300 Ω/sq, and subsequently patterned to a serpentine trace by laser engraving. The resistance of the resulting electrode remains nearly unchanged up to ~80-90% area strain. By applying a voltage of 7 – 9 V to the electrode, the temperature of the BSEP membrane increased to more than 60 °C, well above the polymer's phase transition temperature of 46 °C, thereby lowering its modulus by a factor of 10^3. An electronic Braille device based on the JHEs on a BSEP membrane was assembled with a diaphragm chamber. The electrode was patterned into 3×2 individually addressable pixels according to the standard U.S. Braille cell format. Through Joule heating of the pixels and local expansion of the BSEP membrane using a small pneumatic pressure, the pixels deformed out of the plane by over 0.5 mm to display specific Braille letters. The Braille content can be refreshed for 20,000 cycles at the same operating voltage.

1. Introduction

Soft actuators offer the opportunity for drug delivery, medical surgery,[1,2] designs for actively deformable apparel,[3] soft human–machine interactions,[4] and refreshable Braille display.[5] The essential components for building a soft actuator include the nature of the soft material as a body and the mechanism used to actuate this soft material.[6,7,8] The soft actuator material should be flexible, stretchable as well as reliable, fast, repeatable, and dynamically stable under deformation. It converts an input stimulus into a useful mechanical output. To build the soft actuators, smart materials and structures such as shape memory alloys,[9] dielectric elastomers,[10,11] ionic polymer–metal composites,[12] fibers,[13,14] hydrogels,[15] phase-changes,[5] and magnetic responsive materials[16,17] have been used. Particularly, phase-change materials (PCMs) can change their state when triggered by heat. Their mechanism can be thermal expansion/contraction (e.g., wax-based materials), liquid-to-solid state transformation (e.g., silicone polymer elastomers[6]), an ordered-to-disordered phase transformation (e.g., liquid crystalline elastomers[11]), and thermal transition from the amorphous-to-crystalline state thermal transition (e.g., shape memory polymers). Phase-change polymers containing crystallizable side chains have been shown to combine shape memory with dielectric elastomer actuation.[5,18] These bistable electroactive polymers (BSEPs) are promising for large-strain rigid-to-rigid actuation; however, their operation entails a highly stretchable Joule heating electrode (JHE) to administrate the temperature change.

Carbon nanotubes (CNTs),[19] carbon fibers,[20] graphene,[21] MXene,[22] metallic nanomaterials,[19,23] liquid metals,[24] and conducting polymers have all been reported to fabricate stretchable JHEs.[25,26] High electrical conductivity is required for low-voltage Joule heating. However, achieving highly reversible deformability with preserved low resistance at all strains is difficult.[27] Carbon-based nanomaterials and conductive polymers have medium conductivities [28] which push the input voltage to > 10 V, thereby limiting the application scope of the resulting soft actuators. Metallic nanomaterials have high electrical conductivity but lose their conductive network at high strains and have inferior thermal and oxidation stability.[29] Liquid metal electrodes with low thicknesses can be used for low-power processing systems, but their fabrication is complicated and high stability over time is challenging to obtain.[24]

To achieve large deformation with low resistance change in electrodes, one solution is to use deformable geometries such as wrinkled structures,[15] serpentine patterns,[5] and kirigami.[9] In particular, filamentary serpentine nanomembranes have been shown to exhibit reversible, elastic responses to large strain deformations with low moduli.[30] Another alternative solution is to use combined nanomaterials such as graphene and silver nanowires (AgNWs),[31] or CNTs and silver nanoparticles.[19] However, high-resolution patterning in a stretchable hybrid electrode system is challenging. Consequently, most of the reported deformable JHEs were only bendable, and they rarely could maintain their resistance at strains > 100% (Table S1). In addition, according to the recent literature,[26] most stretchable JHEs based on electroactive nanomaterials were employed as stretchable/wearable heating devices. We previously showed that a serpentine CNT electrode on a BSEP allows up to 188% strain.[5] A soft actuation tactile display was demonstrated, but its operating voltage was above 30 V. Meanwhile, a water-born polymer urethane (WPU)/PEDOT:PSS/rGO hybrid was shown as a JHE up to over 500% strain, but stable Joule heating was obtained only up to 30% strain.[25]

This study introduces a new stretchable JHE for low voltage heating and high thermal stability at various strains up to 100% under a constant voltage. The electrode employed hybrid layers of CNTs and AgNWs embedded in a WPU matrix. A new on-site pre-stretching (OPS) technique was introduced to form wrinkled electrode layers in the actuating areas. The electrode was further patterned into a serpentine trace. The hierarchical JHE was directly formed on a BSEP membrane to provide Joule heating only to the actuating areas. The embedding with WPU enhanced the bonding of the electrode layers with the substrate and protected the conduction pathways in the network during deformation. The new electrode could maintain the same operating voltage for Joule heating at both the actuated and relaxed states. The deformable JHE was incorporated in fabricating a multi-cell refreshable Braille (MCRB). A global pneumatic pressure deformed the locally Joule-heated Braille dots to demonstrate the Braille letters. The MCBR display could maintain a low operating voltage over 20,000 cycles.

2. Results and Discussion

2.1. BSEP membrane as reversible variable stiffness material

BSEP was synthesized from a precursor containing octadecyl acrylate (OA), urethane diacrylate (UDA), and other compounds as shown in Figure S1. The octadecyl side chains in the BSEP crystallized at room temperature leading to a high Young's modulus. They melt above a transition temperature, leading to a modulus reduction by ~10^3. UDA is a long chain difunctional acrylate that forms a crosslinked network structure with OA and thus improves the toughness and elongation at the break of the membrane.[32] To tune the phase transition temperature and modulus change, the composition of all chemicals used in the prepolymer solution of BSEP was formulated to contain 80 weight parts of OA, and 20 parts of UDA. A short chain crosslinker, trimethylolpropane triacrylate (TMPTA), was added at 1.5 parts to increase the tensile strength of the BSEP at the softened state.[33] In addition, 0.5 parts of dimethoxy phenyl-acetophenone (DMPA), and 0.25 parts of benzophenone (BP) were added as photoinitiators in the prepolymer solution. 10 parts of acrylic acid (AA) were added to introduce a reversible crosslinking system and to improve the toughness.[5]

Dynamic mechanical analysis of the BSEP shows a sharp stiffness change from ~10^2 MPa in the rigid state to tens of kPa in the soft state (Figure S2a). The modulus change of three orders of magnitude was reversible. The transition temperature of the BSEP was designed to be approximately 45 – 47 °C so that the required Joule heating energy for the stiffness transition can be reduced while the membrane remains stiff at average environmental temperature and human body temperatures. Figure S2b shows the stress-strain curve of the BSEP membrane at 50 °C. Its elongation at break was at 320% linear strain. The normal tensile strength was 2 MPa, corresponding to a true tensile strength of ~8 MPa, indicative of high toughness to resist tearing or crack formation at high strains. Figure S3 shows the result of the durability test of the BSEP membrane. It endured more than 200,000 actuation cycles without any sign of failure.

2.2 Stretchable Joule heating electrodes

To selectively soften local areas of a BSEP membrane, a JHE was applied to the membrane surface as illustrated in Figure 1. The first step (i) of the process was to attach the BSEP membrane to an air chamber, followed by spray-coating of 0.3 wt% waterborne polyurethane (WPU) solution on the BSEP membrane. The hydrophilic nature of WPU enhances the bonding of CNTs and AgNWs compared to the bare BSEP surface with low surface energy. The sprayed WPU had a rather rough surface (Figure S4a). To smoothen the surface and improve the adhesion, isopropanol alcohol (IPA) was sprayed to wet and dissolve the WPU to allow the polymer to spread out to form a smoother surface (Figure S4b). The roughness (rms value) from atomic force microscopy measurement changed from 2.84 nm to 0.71 nm. WPU was also sprayed as a top layer over the CNTs/AgNWs/CNTs hybrid layers to penetrate the porous networks of CNTs and AgNWs and form a strong bond with the lower WPU layer. This WPU top layer was ~120 nm thick (Figure S5), which was greater than the total thickness of the hybrid layers and thus could completely embed the conductive network. To evaluate the adhesion between the nanomaterials and the WPU matrix, a tape-peeling test was performed (Figure S6). The WPU matrix strongly bonded the hybrid electrode layers to the BSEP substrate. Peeling of the strong Kapton tape did not remove the conductive nanomaterials from the surface. The electrode resistance increased by 7.6% after peeling. It indicates that the nanomaterials have a strong bond with the WPU matrix.

Conventional methods for pre-stretching soft films often involve an additional rigid frame, which requires manual handling of the delicate films, transferring films between different substrates, and complex adhesion requirements between the film and the frame.[34] These methods rarely provide reliable and uniform relaxation. The optical microscopy images in Figure 1 (ii) demonstrate the pre-strained dome on the diaphragm with a 1.5 mm diameter. In our OPS approach, air pressure was used to strain and relax the membrane in a diaphragm fashion. The same air chamber for the operation of the active BSEP membrane was used for pre-stretching of the membrane in the OPS process, which eliminates the need for additional alignment and makes it convenient to transfer or laminate the membrane to different substrates with similarly patterned structure. The finite element analysis (FEA) data shows that the top center area on the actuated membrane had higher stress and strain than the peripheral area (Figure S7). Therefore, unlike the conventional pre-straining methods with the same pre-strain over the entire membrane area,[35] the OPS method can afford localized pre-straining specific to each area. In comparison, conventional method prestretches the entire membrane. Upon relaxation, it is difficult to align the electrodes areas with their respective locations on the pixelated structure of the assembly. Although the percentage of pre-straining may be changed as the application needs, the BSEP membrane in this work was pre-strained to approximately 90%, which was slightly greater than what was required for the targeted actuation height of 0.5 mm.

In step (iii) of Figure 1, after the membrane was cooled to the ambient temperature, layers of CNTs, AgNWs, and CNTs were successively deposited on top of the WPU layer. The top WPU layer was deposited on the pre-strained area (active area) of the electrode to cover and embed the conductive nanomaterials. After the membrane relaxation, wrinkles were formed (iv), and the relaxed areas became opaque showing light scattering from the buckled structure, as shown in Figure 1(iv). To enhance the stretchability of the electrode, the wrinkled active area was patterned into a serpentine trace using laser engraving. Finally, the membrane was gently peeled off the chamber as a free-standing membrane.

The resistance of the electrode active area could be adjusted by spray coating different amounts of CNTs and AgNWs. Although lower resistance led to faster heating and lower driving voltage, it should be compromised for stretchability.[36,37] As the thickness of the CNTs and AgNWs increased, the risk of crack formation near the bus lines could increase. The minimum thickness of the electrode layer was identified by adopting a hybrid layer of CNTs/AgNWs/CNTs (Figure S8). The concentration of the AgNW solution was optimized to 0.01 wt% to make a uniform resistance over the coating substrate. The width and length of the AgNWs are ~41 nm and 15 – 25 μm, respectively (Figure S9). The concentration of the CNT solution was optimized to be 0.03 wt%. The weight ratio of AgNWs to CNTs in the sandwich electrode affected the sheet resistance as shown in Figure S10. At the ratio of 1:3, the hybrid electrode had lower sheet resistance than the homogeneous AgNWs electrode (0.489 kΩ/sq for CNTs/AgNWs/CNTs versus 2.32 kΩ/sq for AgNWs). Also, the concentration of AgNWs impacted on the uniformity of the sheet resistance (Figure S11) and 0.01 wt% showed lower variation in the sheet resistance than 0.02 wt% and 0.04 wt%. The optimized ratio and concentration condition showed the most uniform Joule heating as shown in Figure S12.

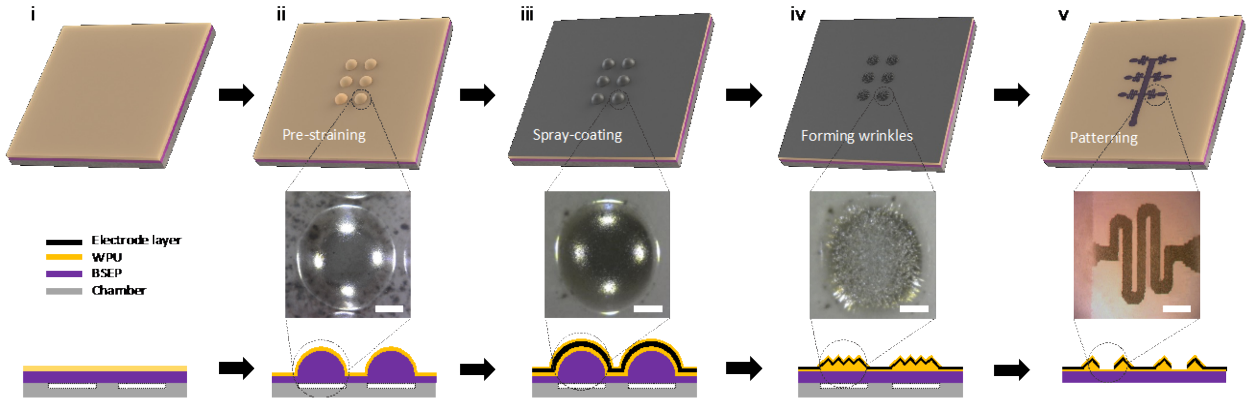

Figure 1. Schematic of the fabrication process of stretchable JHE electrodes. (Middle row) Optical images and (Bottom row) side view of the above schematic. i) The WPU deposition on a BSEP membrane mounted on an air chamber. **ii)** Pre-straining the membrane by pneumatic pressure. **iii)** Spray-coating CNTs/AgNWs/CNTs hybrid electrode layers and a WPU top layer. **iv)** Subsequent release of the membrane, resulting in the formation of wrinkles on its surface. **v)** Patterning the electrode layers employing a laser engraver (scale bars: 600 μm).

Figure 2 shows the scanning electron microscopy (SEM) images of the electrode active layer. The deposition of CNTs on a WPU layer improved the uniformity of the nanotubes on the BSEP membrane (Figure 2a). The AgNWs deposition on the CNT layer was also more uniform than direct deposition on BSEP which has a hydrophobic surface (Figure 2b). The image shows the nanowires coarsely laid on the CNTs layer. The sparsely interconnected AgNW networks were next covered by the densely packed CNTs as shown in Figure 2c. The diameter of the nanowires was approximately 40 nm, whereas the diameter of CNTs was about 0.8 – 2.0 nm. These surface morphologies demonstrated that CNTs bridged the AgNWs network. The CNT layers in the hybrid electrode can be thinner than JHEs using CNTs alone owing to the much higher conductivity of the silver nanowires than CNTs. As shown in Figure S13, hybrid electrodes had more than 90% transparency whereas the CNT electrodes had approximately 80% transparency, indicative of lower total thickness of the conductive layers in the hybrid electrodes.

The hybrid electrode could address the conventional local overheating issues at the inter-nanowire contact points in the AgNW network aforementioned in Figure 2c.[28,29] Figure 2f illustrates a locally actuated JHE. Charge transport occurred in a serpentine-patterned network when the electrode was heated and the BSEP membrane was actuated. The densely distributed CNT network enabled electrons to travel without clogging at the silver nanowire-nanowire junctions, which could reduce the local overheating.

As previously indicated, the embedded hybrid electrode membranes underwent a pre-stretching process to induce wrinkle formation (Figure 2d). This approach leveraged the modulus disparity between the upper nanomaterial layer and the lower layer of WPU on the compliant BSEP layer. To ensure uniform Joule heating voltage requirements during both actuation and relaxation phases, the introduced wrinkles served to maintain the operational voltage irrespective of the initial state of a pneumatic actuator. Figures S14 and S15 provide visual representations of the pre-strained state of the membrane, taking on a dome-like configuration, and the resulting wrinkled structure following the release of pre-strain within the electrode layers and the matrix. The dome structure gives rise to two distinct types of wrinkles: “leg” and “body” wrinkles (Figure

2d (i) and Figure S14(c)). Leg-shaped wrinkles manifested near the dome's periphery, predominantly oriented radially (Figure 2d). They exhibited a regular pattern characterized by a wavelength of approximately 15 μm. Conversely, the central region of the active area underwent wrinkling with biaxial strain, featuring densely packed wrinkles with wavelengths of 5 – 10 μm (Figure 2d (ii)). These induced wrinkles facilitated deformation by unfolding, without subjecting the nanowires and nanotube networks to stretching.

Figure 2e illustrates the status of the wrinkles before and after expansion. Initially, wrinkles exhibited distinct buckling patterns with a wavelength of 5 – 10 μm, arising from an approximate 80 – 90% pre-strain. Nanowires were also distributed along the wrinkle surfaces. Upon subjecting the sample to a 30% area expansion (Figure 2e (i)), the wrinkles experienced slight flattening, resulting in reduced peak heights compared to their pristine state. At 70% strain, the surface was almost completely flattened (Figure 2e (ii)). Figures S16 and S17 show the effect of the wrinkled structure in uniaxial stretching tests, wherein a 50% uniaxial stretching of the electrodes, equivalent to 125% area strain in a biaxial deformation with 50% strain in all directions, did not yield significant elongation in the hybrid electrode network.

These three strategies synergistically can enhance the stretchability of the JHE, making their expanded state beyond the reported deformable JHEs,[26] which are mostly only bendable and will lose their function under high strain deformations. Table S1 presents a comparative overview of our newly developed stretchable electrode in conjunction with existing literature, particularly those that can be concurrently applied to soft actuation systems.

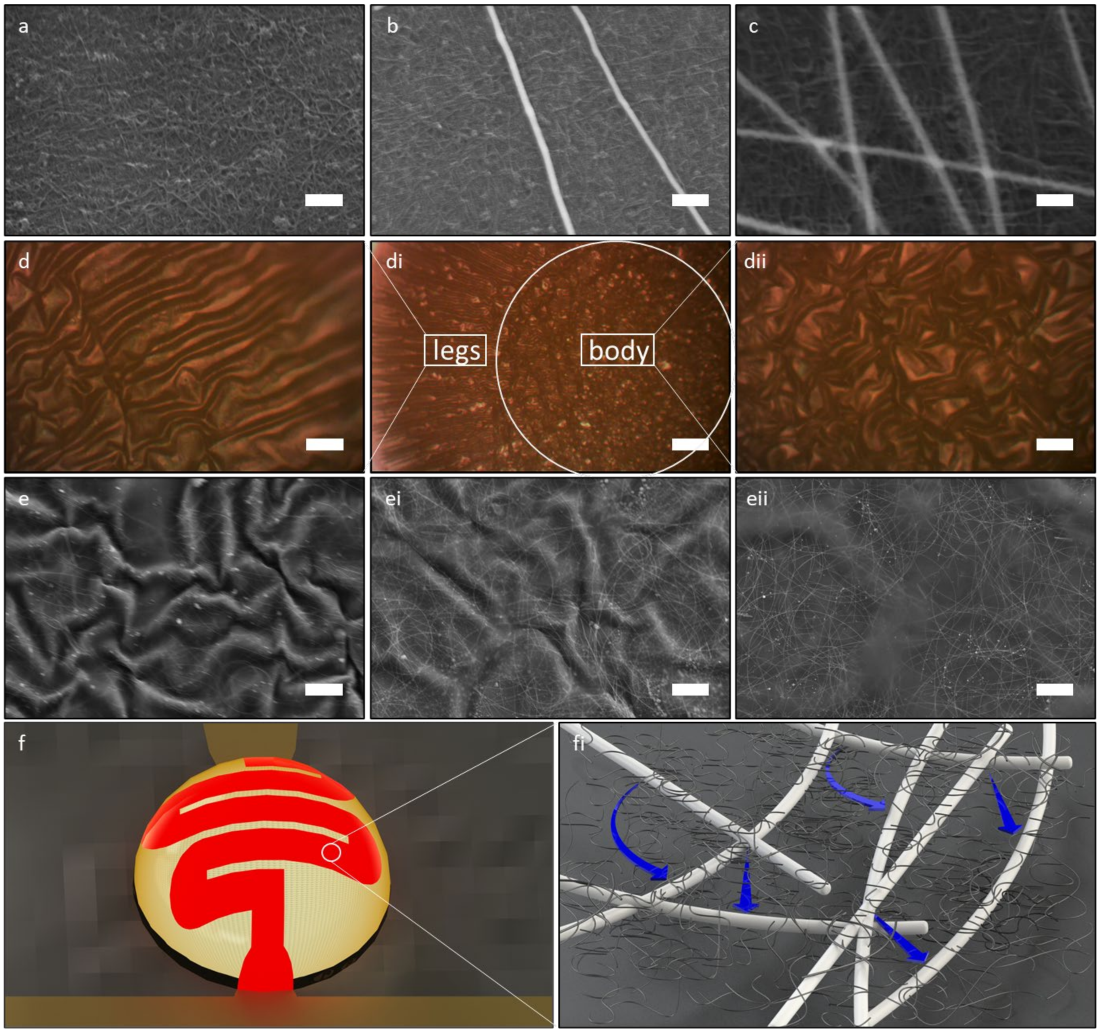

Figure 2. Hybrid electrodes on the BSEP membrane used in the Braille system. Scanning electron microscopy images of the layered **a,** bottom CNTs **b,** AgNWs positioned atop the bottom CNTs, and **c,** top CNTs (scale bars: 300 nm). Optical microscopy images of wrinkles formed during the pre-straining and releasing stages, including **d,** enlarged image of the "legs" area (scale bars: 30 μm), **di,** entire dot area encompassing both the "legs" and "body" regions (scale bars: 100 μm), **dii,** enlarged view of the "body" area (scale bars: 30 μm). Scanning electron microscopy images of the wrinkled hybrid electrode under different area expansion stages **e,** 0% area expansion **ei,** 30% area expansion, and **eii,** 70% area expansion (scale bars: 3.5 μm). **f,** Schematic illustration of a locally actuated JHE and **fi,** charge transport mechanisms within a co-network system comprising a CNTs/AgNWs/CNTs hybrid structure.

2.3 Architecture design for multi-cell refreshable Braille (MCRB)

The deformable JHE was applied to design an electronic Braille (e-Braille). A letter, number, or character in Braille was represented by a specific pattern of raised dots (a.k.a. pixels) in a 3 × 2 array called a cell. E-Braille devices have been proposed using piezoelectric bimorphs,[38,39] shape memory polymers,[40, 46, 47] volume change materials,[41,42] fluidic elastomer actuator arrays,[43] and diverse dielectric elastomer actuators[44] (DEAs). However, these prior approaches have been constrained by their bulky structures, sluggish response times, and/or limited blocking forces. For instance, the manufacturing of fluidic elastomer actuator arrays requires numerous valves, one for each pixel, limiting the feasibility of packing multi-cells in a compact structure. DEAs demand high voltage operation, potentially posing physical and psychological risks to users.[44] Stretchable heater-based e-Braille cells recently reported had low pixel resolution and high driving voltages.[5,45]

Figure 3a illustrates an MCRB display incorporating the stretchable electrodes fabricated in this study. The assembled structure had external dimensions of 70 mm × 150 mm × 10 mm and accommodated 60 pixels in 10 cells. The device comprised a BSEP membrane with the JHE, a printed circuit board (PCB) control panel, adhesive layers, and 3D-printed pneumatic chambers and pins. The active BSEP membrane was laminated between the PCB and a rigid cover. The JHE electrode was patterned to define the individual dot areas. The PCB delivered electrical voltage to each of the electrode areas. Figure S18 shows the layout of the electrical contacts. A miniature pump provided global pneumatic pressure and expanded the Joule heated electrode areas in the BSEP membranes. The sequence of an actuation cycle was shown in Figure 3b. A dot (left in Figure 3b-i) started from its relaxed position and was Joule heated above 48 ºC. The softened area of the BSEP membrane was pneumatically actuated under the applied pneumatic pressure, forming a hemispherical shape that raised the corresponding pin out of the plane (Figure 3b-ii). Upon cooling, the membrane stiffened, while the actuated area remained expanded to maintain the pin at the elevated height (Figure 3b-iii). To revert the pin to its original state, the dot area was heated again, allowing the membrane to relax and the pin to return to its initial position (Figure 3b-iv). The actuation can be repeated, such that the MCRM displays refreshable texts. The MCRM structure was 10 mm thick, the pins measured 1.5 mm in diameter, the dot-to-dot pitch was 2.5 mm, and the cell-to-cell pitch was 6.5 mm, in accordance with standard Braille dimensions.[29]

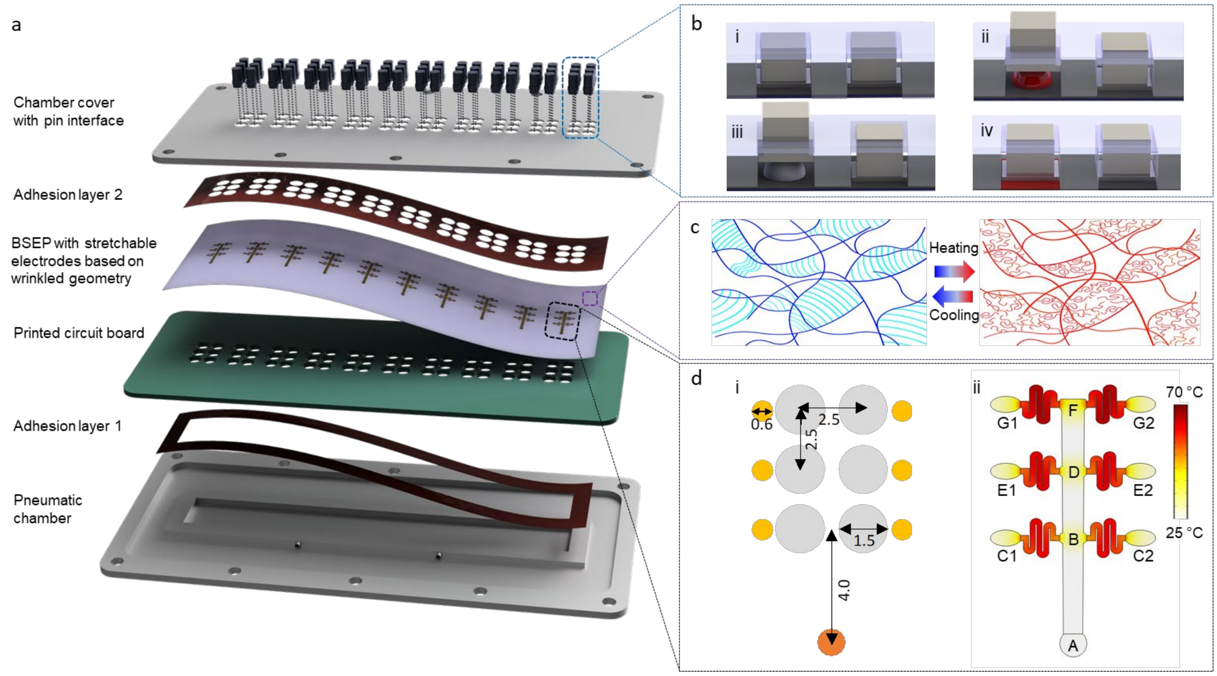

Figure 3. Design and architecture of a Braille display system. a, An exploded-view schematic of a pneumatic actuator-based Braille display featuring a 1×10 cell configuration. **b,** A cross-sectional view delineating the operational mechanism of the device, with a depiction of 2 pixels. **i)** The initial state with all pixels in a relaxed position. **ii)** Actuation of the pixels through the application of Joule heating and air pressure. **iii)** The fixation of the actuated state of the pixels at ambient temperature. **iv)** The return of pixels to a relaxed state. **c,** An illustration of the operational mechanism of the BSEP membrane to be used in Braille display, highlighting its ability to transition between soft and rigid states through heating and cooling. **d, i)** U.S. standard dimension of a single cell, including yellow copper contacts on a PCB. Dimensions and spacing of the pixels correspond to the standard U.S. Braille. **ii)** FEA results of the Joule heating of a serpentine patterned electrode.

The MCRB design exploits the large stiffness change of the BSEP in a narrow temperature range (Figure 3c). At room temperature, the BSEP membrane behaved as a rigid plastic capable of providing a blocking force exceeding 50 g, despite having a thickness of merely 120 μm.[5] It met the requisite blocking force criterion of 15 g for Braille devices, thereby providing enough resistance for users to stably scan and read the Braille.[48] After the transition to the soft state, a low pneumatic pressure of approximately 8 kPa can expand the membrane up to approximately 90% area strain, resulting in a raised height of 0.6 mm. The expanded BSEP membrane raised the pin. This low pressure was optimized based on the thickness of the membrane and the target actuation height.

The hybrid network electrode was patterned into a serpentine trace in each Braille dot area for uniform heating. From a geometrical perspective, the serpentine pattern exhibits low mechanical impedance on electrodes and facilitates efficient Joule heating.[49,50] Figure 3d-i shows the dimension of the dot pattern designed to conform to the U.S. standard dimensions for Braille devices. The heating patterns were simulated by finite element analysis (FEA) of the current density distribution. The electrical current was confined within the winding path of the electrode, resulting in uniform Joule heating along the electrode length. In comparison with the popular spiral pattern often used for Joule heating, the serpentine pattern had a higher conductance of 0.049 S (Figure S19).

Within each Braille cell, the 6 terminal points (**b**, **c**, **d** in Figure S20) had different distances from the ground point (**a**). Figure 3d-ii shows the FEA results of the heating distribution in the serpentine traces. To compensate for the finite resistance on the bus line, the width of the trace was calculated to be between 0.20 and 0.24 mm, ensuring that the resistances in the 6 serpentine traces were identical. Consequently, the 6 dots obtained approximately the same Joule heating temperature under a constant voltage applied between the terminal points and the ground (FEA details are included in Method S1).

2.4. Performance of the heating electrodes in the MCRB display

The operation of the MCRB required the JHE to maintain its resistance in both relaxed and expanded states, allowing for a consistent voltage to heat the BSEP membrane during expansion and recovery. The resistance changes of the electrodes were monitored during actuation cycles using a setup that supplies two voltages, one for the Joule heating and the second for the pneumatic pump (Figure S21). The temperature change was recorded using an infrared camera. Figure 4a and Figure S22 show the resistance evolution of three different serpentine traces with initial resistance of 2.2 kΩ, 3.4 kΩ, and 4.1 kΩ (R1, R2 and R3, respectively), during repeated actuation between 0 and 90% area strains. The measured resistance change between the relaxed and actuated states was 0.1 kΩ, 0.5 kΩ, 0.0 kΩ for R1, R2, and R3, respectively. Other than a slight increase in the initial few cycles, the resistances remained stable. Applying area strain levels below 90% similarly resulted in consistently low resistance change (Figure 4b). However, at 100% strain, there was an approximate 22% increase in resistance, rising from 5.0 kΩ in the relaxed state to 6.1 kΩ in the actuated state. This abnormally large resistance increase was likely caused by excessive deformation beyond the pre-strain level used in the fabrication of the hybrid layers in the electrode. It also confirms the efficacy of the OPS method forming a conductive layer on the wrinkled surface of the BSEP membrane. Note that 58% area strain is the requirement to obtain the 0.5 mm height raise.

The Joule heating stability of the CNTs/AgNWs/CNTs hybrid electrodes is further monitored via temperatures. Figure 4c shows the measured temperatures at the relaxed and actuated state (90% strain) of the three electrodes (R1, R2 and R3) at 9 V. The temperatures were fairly stable, staying between 65 – 68 °C, well above the phase transition temperature of 46 °C. When subjected to different actuation strains, electrodes still maintained each initial temperature of 63, 65, and 68 °C until the end of the actuation at 30%, 50%, and 80% area strains, respectively (Figure 4d). Applying 100% area strain resulted in a 2 °C drop in the actuated state, but the sample returned to the initial temperature of 60 °C after relaxation.

To assess the lifetime of the JHE, repeated actuation to 0.5 – 0.6 mm height with a pneumatic pressure of approximately 8 kPa was performed at 7.7 V (Figure 4e). The resistance of the electrode increased from 2.2 kΩ to 3.3 kΩ after 20,000 actuation cycles (Figure S23). At the constant voltage of 7.7 V, the temperature generated from Joule heating gradually decreased from 66 ºC to 54 ºC after 20,000 cycles. The final temperature remained higher than the transition temperature of the membrane.

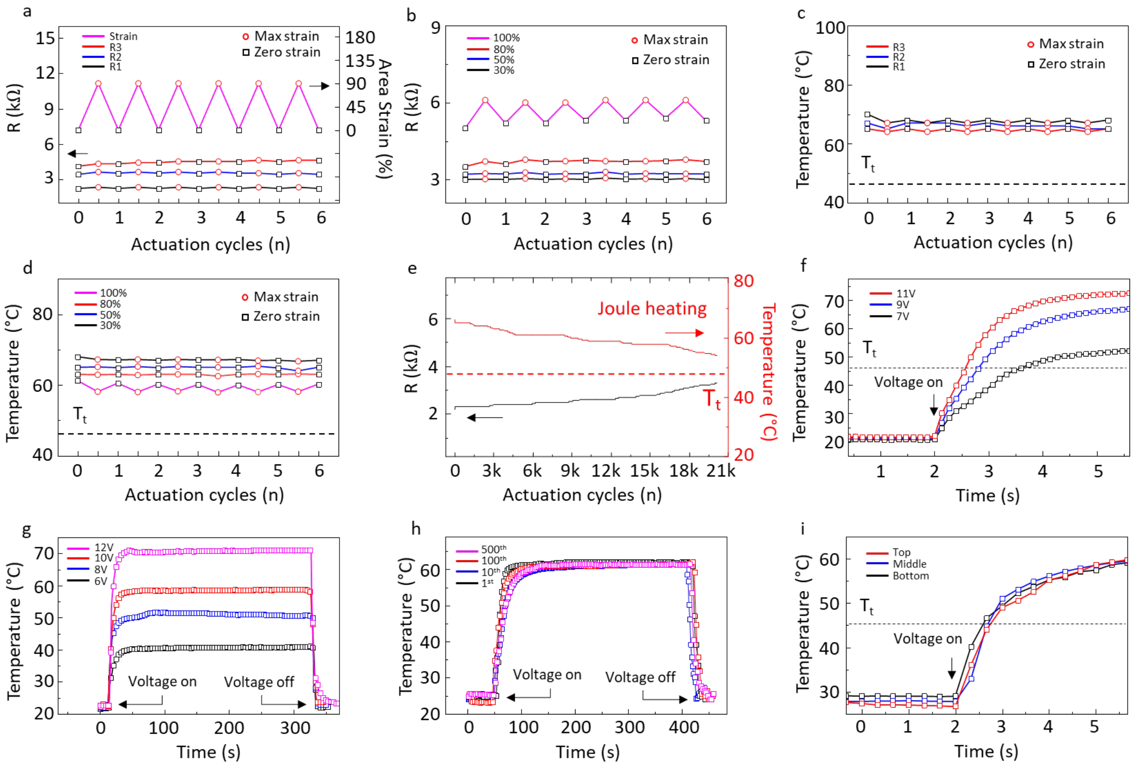

Figure 4. Joule heating and electromechanical performance of the electrodes used in the Braille display system. a, Resistance change of the CNTs/AgNWs/CNTs hybrid electrodes with different initial resistances (R1= 2.2 kΩ, R2= 3.4 kΩ, R3= 4.1 kΩ) over six actuation–relaxation cycles (left axis). The curve of area strain applied during the actuation cyclic test, with a peak strain of 90% (indicated by red circles) and 0% in the relaxed state (indicated by the black square) (right axis). **b,** Resistance change under different area strains during actuation, including 30%, 50%, 80%, and 100%. **c,** Joule heating temperature change of the electrodes with various initial resistance (R1= 2.2 kΩ, R2= 3.4 kΩ, R3= 4.1 kΩ), with T_t representing the phase transition temperature of the BSEP membrane. **d,** Joule heating temperature change in response to actuation area strains of 30%, 50%, 80%, and 100%. **e,** Resistance and temperature change of the electrode during repeated actuation and relaxation tests under the same applied voltage of 7.7 V. **f,** Transient temperature rise of the electrode with 3.0 kΩ during Joule heating curves at different applied voltage of 7, 9, and 11 V. **g,** Transient temperature curve of a Braille dots during Joule heating voltage activation and deactivation at various applied voltages of 6, 8, 10 and 12 V. **h,** Transient temperature curve during specified actuation cycles to 80% area strain, with a heating voltage of 10 V. **i,** Transient temperature curve of the top, middle, and bottom dots within a 3 × 2 cell (see Figure 3d).

The speed of Joule heating plays a key role in determining the refreshing rate of the MCRB.[51,52] Figure 4f displays the temperature evolution of the electrode within Braille dots at 7, 9, and 11 V. It took 1.2, 0.6, and 0.4 s to reach the phase transition temperature of 46 °C at 7, 9, and 11 V, respectively. As shown in Figures S24(a) and (b), the pneumatic pressure could expand the membrane within 1 s, and the membrane stiffened within 1 s as it was cooled below 40 °C. The laser displacement sensor showed that the actual pins were displaced within 1 s and released back to their original state within 0.5 s. Therefore, the total refreshing rate was less than 1.5 s. Based on 9 V operating voltage, the power consumption of Joule heating cell was calculated to be 0.155 W (Figure S25).

Figure 4g shows the temperature beyond the initial rise at constant voltages. Following the initial rapid rise, the temperature reached an equilibrium value, and remained constant for 5 min until the driving voltage was removed from the electrode at the relaxed state. This result confirmed the heating stability of the JHE in MCRB. Figure 4h shows the temperature profiles in the 1st, 10th, 100th, and 500th actuation cycles at 80% area strain with an applied voltage of 10 V. There was no significant temperature change after 500 actuation cycles. Each temperature point was measured after the membrane returned to its relaxed state. Figure 4i shows a comparable Joule heating among the dots within a unit cell. With resistance finely tuned by electrode pattern design depicted in Figure S20, every dot within a cell reached the phase transition temperature in 0.5 s when subjected at 9 V. This consistent response at the cell level ensured uniformity across the entire MCRB display array.

2.5. Demonstration of an MCRB display

Figure 5 illustrates a 1 × 10 cell array MCRB. The hybrid JHEs on a BSEP membrane with serpentine pixel patterns were laminated onto the PCB board such that the contact points on the electrode overlapped with the copper contacts on the PCB. The assembly was sealed within an air chamber connected to a pneumatic micropump with specific dimensions. The testing of Joule heating was initiated by applying 10 V to selected dots via the PCB. The pixels subjected to the voltage were heated to temperatures exceeding 60 °C. Figure 5a displays the IR image of the 1 × 10 Braille cell array corresponding to 'ucla smrl' in Braille language. The temperature rise was uniform among all the activated pixels. Figure 5b shows the top-view optical image of the array under pneumatic pressure of approximately 9 – 10 kPa. The actuation height of the heated dots was measured to be around 0.6 mm, corresponding to an area strain of 81.3%. A 3D-printed top cover (dimensions: 70 mm × 150 mm × 0.7 mm) with pins, aligned with the through holes, was placed over the BSEP membrane and screw-tightened with the pneumatic chamber beneath the PCB board. The positions of the pins and the serpentine traces were vertically aligned. Figure 5c depicts the array with pins over the actuated BSEP dots, causing them to be raised. After the heating voltage was removed, the dots remained elevated, and the position was maintained after the pump was turned off (Figure 5d). When the BSEP membrane returned to ambient temperature, and the pump was turned off, the raised pins remained their elevated state and could support up to 50 g of force. The contents were erased when the JHE was reheated without the pump pressure. Then the pins returned to their lowered state, completing the refresh cycle of the Braille display (Figure 5e).

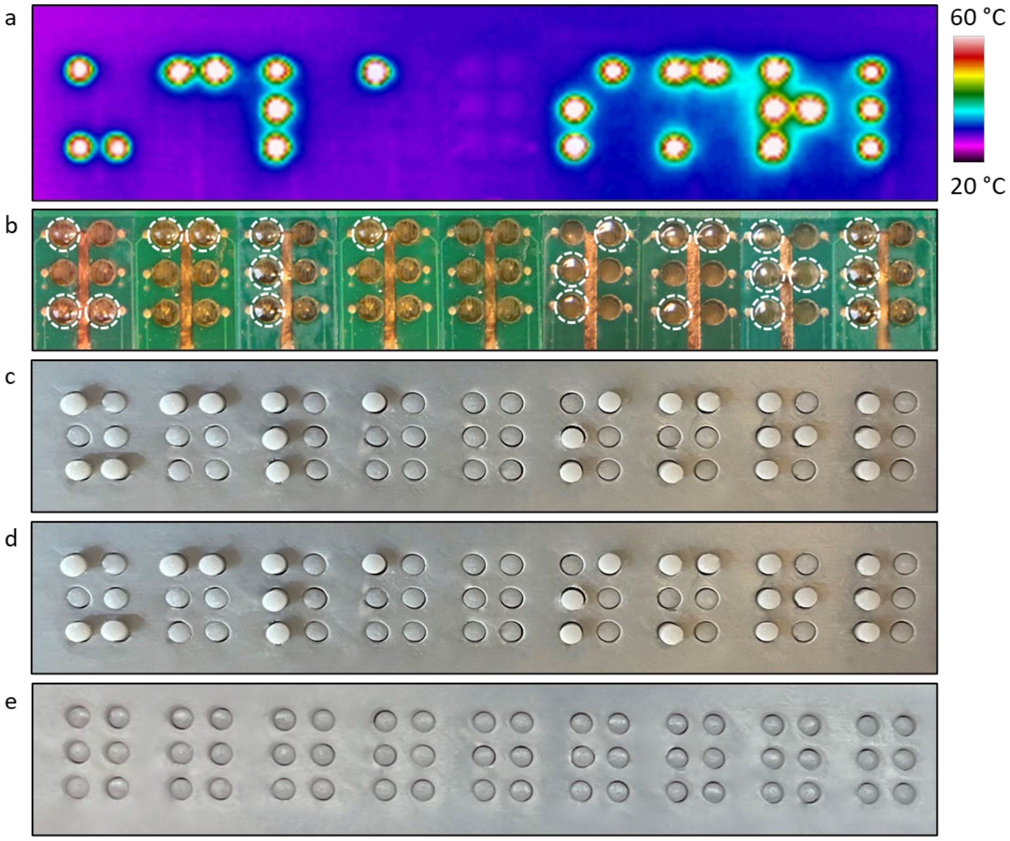

Figure 5. Demonstration of the letters 'ucla smrl' in Braille with the CNTs/AgNWs/CNTs hybrid JHEs. a, IR thermal image of the Braille dots heated above the transition temperature of the BSEP membrane by 1st Joule heating at 10 V. **b,** Optical image of the heated dots actuated by an air pressure of 9 – 10 kPa. Activated dots are marked with white dashed circles. **c,** Braille pins raised as a result of the actuated BSEP diaphragms. **d,** Braille pins that remained raised even after the heating voltage and the pump were turned off. **e,** Braille pins at the relaxed state after 2nd Joule heating with no pneumatic pressure applied.

3. Conclusion

A stretchable, patternable, and low-voltage operating JHE has been developed using CNTs/AgNWs/CNTs hybrid layers. The on-site pre-stretching (OPS) approach was effective in creating Joule heaters locally at the active areas of the BSEP membrane. The incorporation of a buckled structure and serpentine patterning of the hybrid layers ensured a strain-invariant stretchability. Moreover, embedding the CNTs/AgNWs/CNTs electrode within a WPU matrix enhanced its adhesion to the substrate and allowed for reversible stretchability of the electrode. The Joule heaters exhibited consistent performance with the same voltage at both actuated and relaxed states, enduring more than 20,000 actuation cycles. By using the localized Joule heating of individual dots in combination with globally applied pneumatic pressure, a 1 × 10 Braille cell array was demonstrated.

4. Experimental Section

CNTs, AgNWs, and WPU solution: 8 mg P3 SWCNT functionalized with carboxylic groups (Carbon Solution Inc) was dispersed into 2 ml deionized (DI) water and 18 ml ethanol (EtOH). The solution was bath-sonicated for 120 min, then centrifuged at 9000 rpm for 18 min. The supernatant CNT solution was used for spraying. A 1 ml of 1 wt% diluted AgNW solution (Kechuang Inc) was diluted with 9 ml of isopropyl alcohol (IPA). The mixture was agitated to ensure homogeneity. The solution was centrifuged at 5500 rpm for 10 min to facilitate the removal of the supernatant. Subsequently, 10 ml of EtOH was added to make a 0.1 wt% AgNW solution with agitation. The solution underwent filtration and further dilution to attain the requisite concentration for the experiment. A 35 wt% diluted water-borne polyurethane (WPU, Bond Polymers International) was further diluted by IPA to yield a 0.3 wt% solution. Stirring for 1 hour ensured uniformity in the resulting solution. The prepared solutions detailed above were utilized for subsequent experimental procedures.

Preparation of BSEP membranes: BSEP synthesis involved the use of octadecyl acrylate (OA, Aldrich, *Mw* 324.54) for crystallization at room temperature and urethane diacrylate (UDA, Sartomer) to enhance elongation at the break. The final prepolymer composition for BSEP is comprised of 80 weight parts OA, 20 parts UDA, 10 parts acrylic acid (AA, Aldrich), 1.5 parts trimethylolpropane triacrylate (TMPTA, Aldrich), 0.5 parts dimethoxy phenyl-acetophenone (DMPA, Aldrich), and 0.25 parts of the benzophenone (BP, Aldrich). The prepolymer solution was injected between two slide glasses, using a spacer thickness of 120 μm.

Laser Cutting and Engraving: The hybrid electrodes underwent laser engraving using an engraver (Epilog FiberMark Model 8000) to create a serpentine pattern, with parameter adjustments based on material layer thicknesses. Additional membrane components such as adhesion layer 2, WPU deposition face masks, and gold sputtering substrates were produced using a laser cutter (Epilog Zing Model 10000). Laser settings were fine-tuned according to specific material properties.

Finite Element Analysis (FEA): COMSOL software facilitated FEA to model Joule heating uniformity and current density distribution across various patterns. A description of material properties, boundary conditions, and equations were described in each simulation result and detailed under Method 1.

Characterization: Optical images were acquired using an optical microscope (TFProbe, SP200MS) at varying magnification. Membrane thicknesses were determined using a surface profiler (Veeco Dektak 8 Profilometer) and an AFM (Bruker Dimension FastScan SPM). The mechanical properties of the materials were characterized by using Dynamic Mechanical Analysis (DMA, TA Instruments RSAIII). An IR camera and Kiethley conductivity device were used to measure changes in temperature and resistance during the actuation. Dynamic temperature sweep tests were performed by ramping the temperature at a rate of 2 °C/min and a frequency of 1 Hz, spanning from 25 to 60 °C. Samples measuring 8 mm in width and 120 μm in thickness were analyzed using DMA, utilizing an 8 mm gap between thin membrane grips. Stress-strain curves of the BSEP membrane were measured at 50 °C with a strain rate of 0.1 mm/s. The structure of hybrid electrodes and the evolution of wrinkle expansion under varying applied strains were observed and confirmed using SEM (ZEISS Supra 40VP). Transmittance measurements for comparison between hybrid and homogeneous electrodes were measured by UV-vis spectrophotometer (Shimadzu). The evaluation of actuation performance involved monitoring changes in resistance using a Keithley 2400 analyzer and tracking temperature variations through a thermal IR camera (ICI Inc, 9320P).

Supporting Information

Supporting Information is available from the Wiley Online Library or from the author.

Acknowledgments

The work was supported by the National Institute of Health (Award number 1R01EY030246). The authors acknowledge the use of instruments at the Electron Imaging Center for NanoMachines supported by NIH (1S10RR23057 to ZHZ) and CNSI at UCLA. J.K. and H.H. acknowledge fellowship support from UCLA.

Conflict of Interest

The authors declare no conflict of interest.

Keywords

Stretchable electrodes, Joule heating, Braille devices, pneumatic actuation, bistable electroactive polymers.

Reference

[1] J. Di, S. Yao, Y. Ye, Z. Cui, J. Yu, T. K. Ghosh, Y. Zhu and Z. Gu, *ACS Nano*, **2015**, *9*, 9407.

[2] T. Ranzani, G. Gerboni, M. Cianchetti and A. Menciassi, *Bioinspir Biomim*, **2015**, *10*, 035008.

[3] B. Holschuh, E. Obropta and D. Newman, *IEEE/ASME Transactions on Mechatronics*, **2015**, *20*, 1264.

[4] M. T. Holley, N. Nagarajan, C. Danielson, P. Zorlutuna and K. Park, *Lab Chip*, **2016**, *16*, 3473.

[5] Y. Qiu, Z. Lu and Q. Pei, *ACS Appl Mater Interfaces*, **2018**, *10*, 24807.

[6] D. J. Kang, S. An, A. L. Yarin and S. Anand, *Nanoscale*, **2019**, *11*, 2065.

[7] L. Somm, D. Hahn, N. Kumar and S. Coros, *IEEE Robotics and Automation Letters*, **2019**, *4*,761.

[8] C. Tawk and G. Alici, *Advanced Intelligent Systems*, **2021**, *3*, 75.

[9] H. Jin, E. Dong, M. Xu, C. Liu, G. Alici and Y. Jie, *Smart Materials and Structures*, **2016**, *25*, 085026.

[10] E. Askounis, Y. Shi, R. Plamthottam, T. Libby, Z. Peng, K. Youssef, J. Pu, R. Pelrine, Q. Pei, *Science* **2022**, *377*, 228.

[11] D. McCoul, S. Rosset, N. Besse and H. Shea, *Smart Materials and Structures*, **2017**, *26*, 125022.

[12] Y. Bahramzadeh and M. Shahinpoor, *Soft Robotics*, **2014**, *1*, 38.

[13] X. Duan, J. Yu, Y. Zhu, Z. Zheng, Q. Liao, Y. Xiao, Y. Li, Z. He, Y. Zhao, H. Wang and L. Qu, *ACS Nano*, **2020**, *14*, 14929.

[14] Y. Yang, Y. Wu, C. Li, X. Yang and W. Chen, *Advanced Intelligent Systems*, **2019**, *2*, 1900077.

[15] G. Lee, M Zarei, Q. Wei, Y Zhu, SG Lee, Small **2022**, *18*, 2203491.

[16] L. Wang, C. F. Guo and X. Zhao, *Extreme Mechanics Letters*, **2022**, *51*, 101604.

[17] Y. Kim and X. Zhao, *Chem Rev*, **2022**, *122*, 5317.

[18] Z. Ren, W. Hu, C. Liu, S. Li, X. Niu, and Q. Pei, *Macromolecules* **2016**, *49*, 134.

[19] N. Anusak, J. Virtanen, V. Kangas, V. Promarak and P. Yotprayoonsak, *Thin Solid Membranes*, **2022**, *750*, 139201.

[20] J. G. Kang, G. Wang and S. K. Kim, *Materials (Basel)*, **2020**, *13*, 5255.

[21] H. Kim, S. Lee and H. Kim, *Sci. Rep.*, **2019**, *9*, 1511.

[22] Q.-W. Wang, H.-B. Zhang, J. Liu, S. Zhao, X. Xie, L. Liu, R. Yang, N. Koratkar and Z.-Z. Yu, *Adv.*

Func. Mater., **2019**, *29*, 20.

[23] T. B. Song, C. Chung, Y. Yang, B. Bob, H. Duan, G. Li, K. Tu, Y. Huang, and Y. Yang, *ACS nano*, **2014**, *8,* 2804.

[24] J. Dong, X. Tang, Y. Peng, C. Fan, L. Li, C. Zhang, F. Lai, G. He, P. Ma, Z. Wang, Q. Wei, X.-P. Yan, H.-L. Qian, Y. Huang and T. Liu, *Nano Energy*, **2023**, *108*, 1319.

[25] R. Zhou, P. Li, Z. Fan, D. Du and J. Ouyang, *Journal of Materials Chemistry C*, **2017**, *5*, 1544.

[26] M. O. Faruk, A. Ahmed, M. A. Jalil, M. T. Islam, A. M. Shamim, B. Adak, M. M. Hossain and S. Mukhopadhyay, *Appl. Mat. Today*, **2021***, 23,* 12726.

[27] Y. Wu, J. Xiang, C. Yang, W. Lu, C. M. Lieber, *Nature* **2004**, *430*, 61.

[28] Y. Ahn, Y. Jeong, Y. Lee, ACS. *Appl. Mater. Interfaces* **2012**, *4*, 6410.

[29] T. Kim, Y. W. Kim, H. S. Lee, H. Kim, W. S. Yang, K. S. Suh, *Adv. Funct. Mater.* **2013**, *23*, 1250.

[30] D. Kim, J. Bang, W. Lee, I. Ha, J. Lee, H. Eom, M. Kim, J. Park, J. Choi, J. Kwon, S. Han, H. Park, D. Lee and S. H. Ko, *Journal of Materials Chemistry A*, **2020**, *8*, 8281.

[31] G. Lee, SG Lee, Y Chung, GY Bae, S Lee, S. Ryu, K. Cho, Adv. Electron. Mater. **2016**, *2*, 1600158.

[32] Z. Ren, W. Hu, C. Liu, S. Li, X. Niu, and Q. Pei, *Macromolecules* **2016**, *49*, 134.

[33] X. Niu, H. Stoyanov, W. Hu, R. Leo, P. Brochu, and Q. Pei, *J. Polym. Sci., Part B: Polym. Phys.* **2013**, *51*, 197.

[34] H. R. Choi, K. Jung, N. H. Chuc, M. Jung, I. Koo, A. Hyouk, R. Choi, J. Koo, J. Lee, J. Lee, J. Nam, M. Cho, Y. Lee, *Smart Struct. and Mater.* **2005**, *5759*, 282.

[35] X. Wang, J. Li, H. Song, H. Huang, J. Gou, *ACS. Appl. Mater. Interfaces* **2018**, *10*, 7371.

[36] S. Shajari, S. Ramakrishnan, K. Karan, L. J. Sudak and U. Sundararaj, *Appl. Mater. Today*, **2022**, *26*, 101295.

[37] G. J. N. Wang, A. Gasperini, Z. Bao, *Adv. Electron. Mater.* **2018**, *4*, 1700429.

[38] N. Runyan, D. Blazie, *Proc. SPIE. Electroactive Polymer Actuators and Devices* **2010**, *7642*, 764207.

[39] D. G. Seo, Y. H. Cho, *J. of Mechanical Sci. and Tech.* **2018**, *32*, 631.

[40] R. Velazquez, E. E. Pissaloux, M. Hafez, J. Szewczyk, *IEEE Trans Instrum. Meas.* **2008**, *57*, 1051.

[41] H. J. Kwon, S. W. Lee, S. S. Lee, *Sen. Act. A Phys.* **2009**, *154*, 238.

[42] J. S. Lee, S. Lucyszyn, *J. of Microelectromechanical Sys.* **2005**, *14*, 673.

[43] HaptX: Haptic gloves for virtual reality and robotics. https://haptx.com/technology/. Accessed 15 May 2021.

[44] Z. Yu, W. Yuan, P. Brochu, B. Chen, Z. Liu, and Q. Pei, *Appl. Phys. Lett.* **2009**, *95*, 192904.

[45] N. Besse, S. Rosset, J. Zarate, and H. Shea, *Adv. Mater. Technol.* **2017**, *2*, 1700102.

[46] T. Chung, A. Romo-Uribe, P. T. Mather, *Macromolecules* **2008**, *41*, 184.

[47] Z. Yu, W. Yuan, P. Brochu, B. Chen, Z. Liu, Q. Pei, *Appl. Phys. Lett.* **2009**, *95*, 192904.

[48] N. H. Runyan, F. Carpi, *Expert Rev. Med. Devices* **2011**, *8*, 529.

[49] D. H. Kim, N. Lu, R. Ma, Y. S. Kim, R. H. Kim, S. Wang, J. Wu, S. M. Won, H. Tao, A. Islam, K. J. Yu, T. il Kim, R. Chowdhury, M. Ying, L. Xu, M. Li, H. J. Chung, H. Keum, M. McCormick, P. Liu, Y. W. Zhang, F. G. Omenetto, Y. Huang, T. Coleman, J. A. Rogers, *Science* **2011**, *333*, 838.

[50] Y. Zhang, Z. Yan, K. Nan, D. Xiao, Y. Liu, H. Luan, H. Fu, X. Wang, Q. Yang, J. Wang, W. Ren, H. Si, F. Liu, L. Yang, H. Li, J. Wang, X. Guo, H. Luo, L. Wang, Y. Huang, J. A. Rogers, *Proc. Natl. Acad. Sci.* **2015**, *112*, 11757.

[51] A. Russomanno, S. O'Modhrain, R. B. Gillespie, M. W. M. Rodger, *IEEE Trans. Haptics* **2015**, *8*, 287.

[52] T. Hu, S. Xuan, Z. Xu, S. Sun, J. Li, X. Gong, *Adv. Mater. Tech.* **2022**, *7*, 2100777.

Supporting Information for

Deformable Joule heating electrode based on hybrid layers of silver nanowires and carbon nanotubes and its application in a refreshable multi-cell Braille display

Jinsung Kim, Zhixin Xie, Zihang Peng, HyeonJi Hong, Shaghayegh Shajari, Yuxuan Guo, Hanxiang Wu, Yuan Meng, Roshan Plamthottam, Yuan Zhu, Yu Qiu, Huiying Wang, Alex Cheng, and Qibing Pei*

J Kim, Z Xie, Z Peng, HJ Hong, S Shajari, Y Guo, H Wu, Y Meng, R Plamthottam, Y Zhu, Y Qiu, H Wang, A Cheng, and Q Pei
Soft Materials Research Laboratory, Department of Materials Science and Engineering
Henry Samueli School of Engineering and Applied Science
University of California
Los Angeles, 420 Westwood Plaza, Los Angeles, CA 90095, USA
E-mail: qpei@seas.ucla.edu

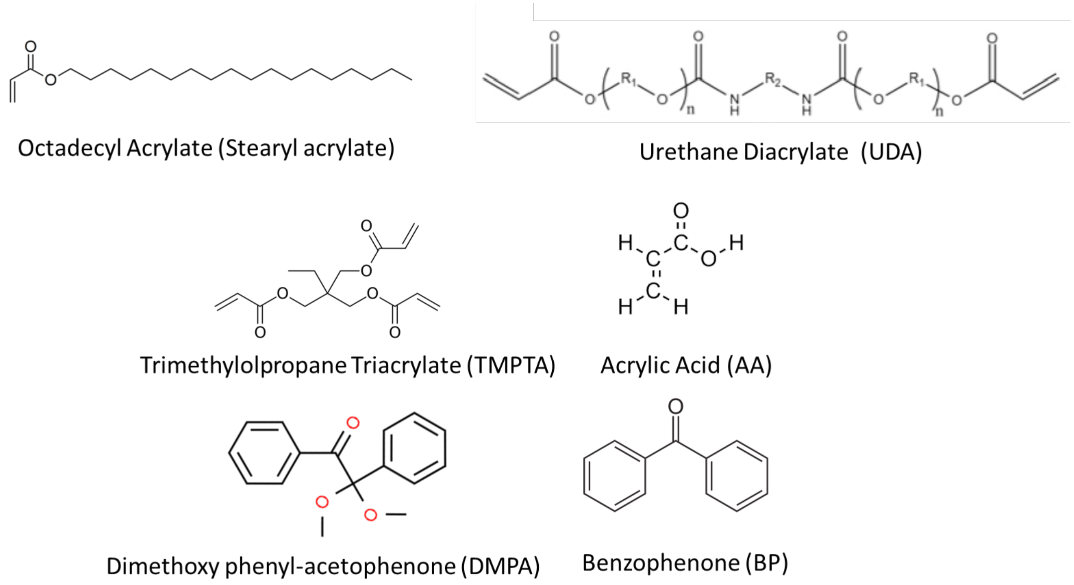

Figure S1. Chemical structure of monomers and photoinitiators employed for BSEP synthesis. Octadecyl acrylate (OA) and urethane diacrylate (UDA) are the primary domains in phase-changing polymer networks. Typical composition of the prepolymer solution contains 80 parts OA, 20 parts UDA, 1.5 parts TMPTA, 0.5 parts DMPA, and 0.25 parts BP, 10 parts acrylic acid.

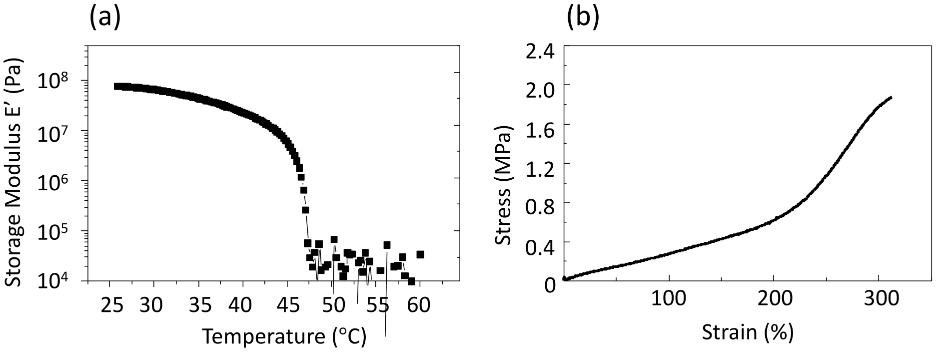

Figure S2. Mechanical Properties of the BSEP membrane. (a) The storage modulus versus temperature profile of the BSEP membrane. **(b)** The stress-strain curve of the BSEP membrane at 50 °C, tested at a stretching rate of 0.1 mm/s.

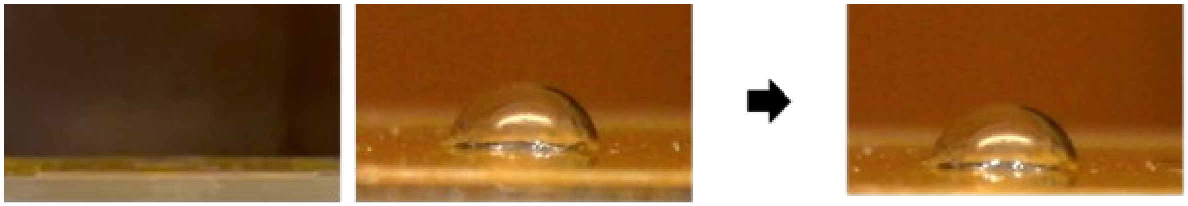

Off state

On state

On state after 200,000 cycles

Figure S3. Optical microscopic images of a BSEP membrane (diaphragm architecture) during a 200,000-cycle actuation test. Applying pneumatic pressure between 10 and 12 kPa induced a 100% area strain, equivalent to Braille dots measuring 0.7 to 0.8 mm in height. A complete actuation cycle took 2 seconds to actuate (switching on the dot) and 1 second to relax (switching off the dot).

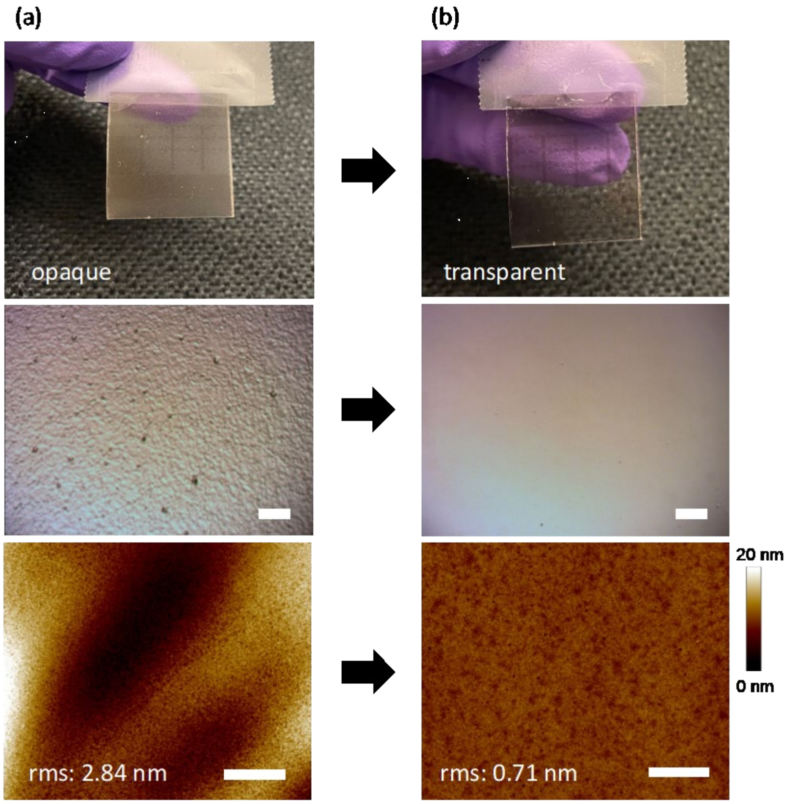

Figure S4. Photographs for the effect of the solvent treatment. (a) Freshly sprayed WPU and **(b)** after spraying IPA and subsequent drying of the solvent. (scale bar : 300 nm (second row), 1μm (third row))

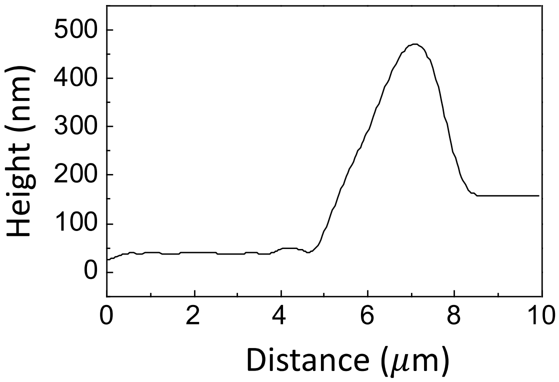

Figure S5. Thickness measurement using Atomic Force Microscopy (AFM). A deposition of 0.6 ml of a 0.3 wt% WPU solution was sprayed onto the glass substrate and allowed to dry for 10 minutes. Subsequently, the dried film thickness was measured in tapping mode AFM.

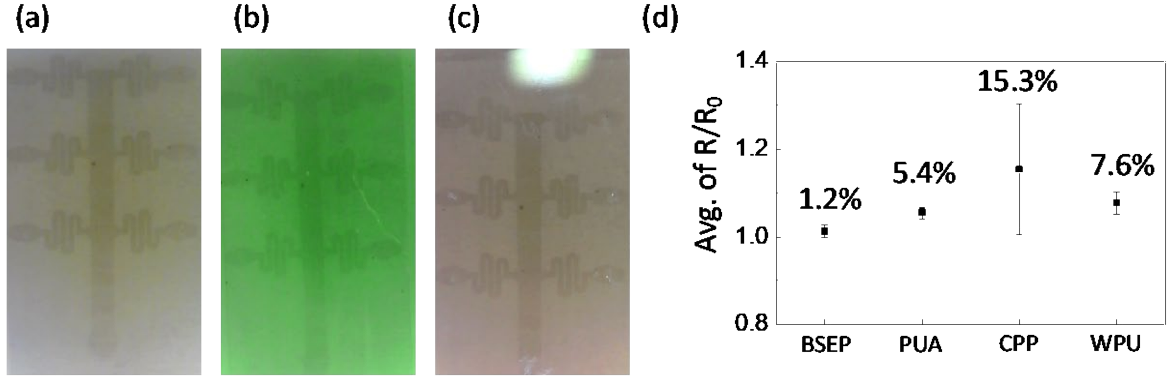

Figure S6. **Adhesion test to assess bonding of the nanomaterials by the WPU layer. (a)** Before the Kapton tape was laminated, **(b)** after the tape was laminated, **(c)** after peeling off of the tape, and **(d)** average resistance change of the CNTs/AgNWs/CNTs hybrid electrode embedded in specified polymers before and after tape peeling test. The Kapton tape has a peeling strength of 46 oz/in. CPP is a dielectric elastomer formulated from CN990, propoxylated neopentyl glycol diacrylate, poly propylene glycol acrylate, and acrylic acid. The tape-peeling test started by measuring the initial resistance of the electrodes embedded in four different matrices, BSEP, PUA, CPP, and WPU. Afterward, a Kapton tape was tightly laminated onto each sample without any trapped air bubbles. The resistance was measured again after peeling off the tape.

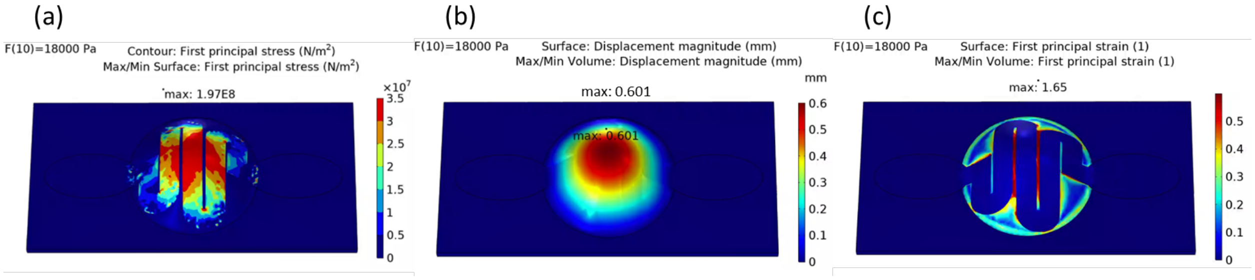

Figure S7. 3D Finite Element Analysis (FEA) for the stress (a), out of plane displacement (b), and strain of the electrode (c), under pneumatic pressure.

In Figure (a), the stress over the active area varies from 0 to 1.97E8 N/m^2. The center of the patterned electrode experienced the highest stress, consistent with the experimental results showing the vulnerability of the center lines to breakage. In Figure (b), the applied pressure resulted in a maximum film actuation of 0.6 mm at the center. Discrepancies between simulated and experimental pressures arose from simulation boundary limitations. In simulation, a distinct modulus difference between the heated and non-heated areas is applied, whereas in reality, the heating gradually diffuses along the boundary. Also, simulated nanomaterial thickness exceeded practical limits, suggesting that achieving the same strain in reality would require less pneumatic pressure. Figure (c) shows a maximum strain change of 1.65 over the active area. The simulation utilized a solid mechanics model with pressure sweeping from 0 to 18 kPa. Material parameters used in the simulation were as follows: CNT (E:1E9 Pa, v: 0.35, ρ: 1.3 kg/m^3), BSEP matrix layer (E:7E5 Pa, v : 0.49, ρ : 1.5 kg/m^3, t: 100 μm)

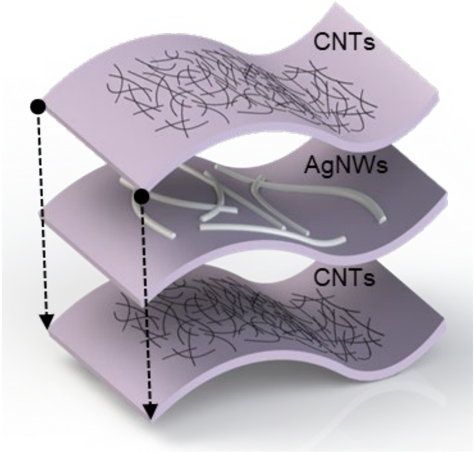

Figure S8. Hybrid structure of Joule heating electrodes. The heating electrodes comprise a hybrid network of two CNT layers sandwiching an AgNWs layer (CNTs/AgNWs/CNTs). The CNT, AgNW, and CNT layers were spray coated sequentially. This hybrid system produced low electrode resistance at a low total thickness for high mechanical compliancy. Also, it has a higher thermal stability by improving the high contact resistance issue at AgNW junctions.

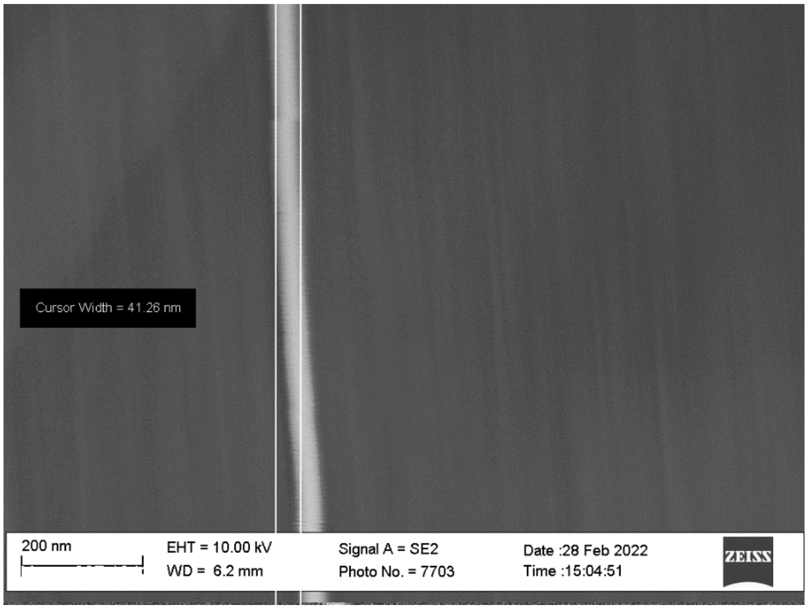

Figure S9. Scanning electron microscopy image for a silver nanowire. Its width is about 41 nm. (scale bar: 200 nm)

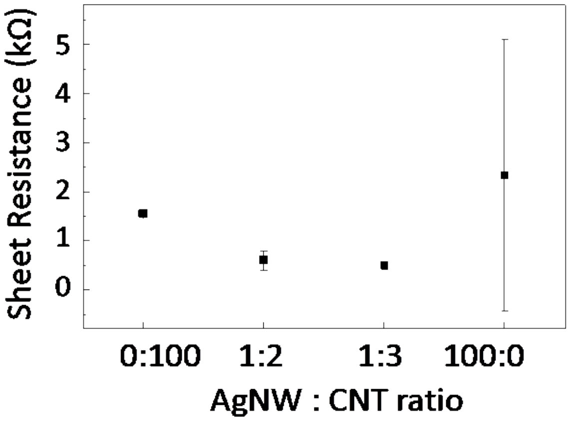

Figure S10. The sheet resistance of the CNTs/AgNWs/CNTs electrodes as a function of the ratio between AgNWs and CNTs. The concentration of AgNW solution was fixed at 0.01 wt% with 3.5 ml for spraying. Also, 2 ml and 3 ml of 0.035 wt% CNT solution were sprayed for 1:2 and 1:3 ratio samples, respectively. For the homo CNT electrode, a 15 ml volume was used. Homo AgNWs electrode has a substantial deviation in sheet resistance, ranging from 420 Ω/sq to 6.8 kΩ/sq within a substrate, possibly due to non-conductive voids among the nanowires.[1] In contrast, homo CNT electrodes demonstrate the highest uniformity with the minimal deviation. Employing the hybrid electrodes with AgNWs and CNTs reduces the variation of the sheet resistance. A higher AgNW : CNT ratio (1:3) enhances sheet resistance uniformity compared to a 1:2 ratio. Hybrid electrodes exhibit even lower resistance than homo AgNW electrodes because the CNTs effectively connect the junctions of silver nanowires, allowing more current paths.

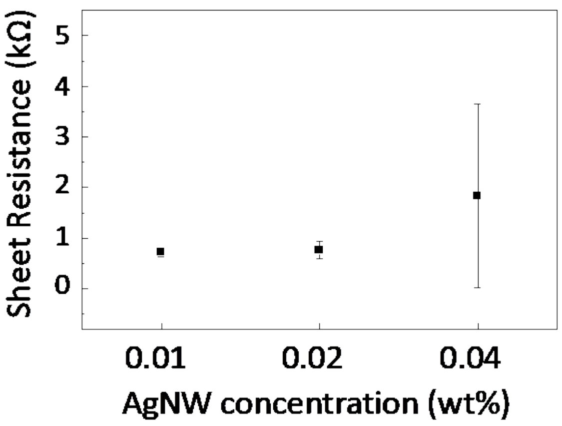

Figure S11. A sheet resistance of the electrodes as a function of AgNW concentration from 0.01 wt% to 0.04 wt%. Higher AgNWs solution concentration leads to increase in sheet resistance variation. Conversely, reducing the AgNWs concentration and increasing the number of spraying paths significantly improve the variation. The ratio between AgNWs and CNTs was fixed at 1:2. The total amount of the used AgNWs volume was also fixed at 0.33 mg.

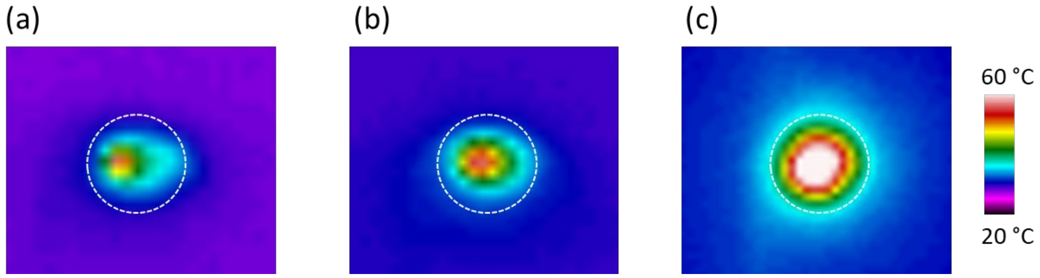

Figure S12. IR thermal image of the Joule heating electrodes showing different heating uniformity with different concentration of AgNWs and the ratio between CNTs and AgNWs. 9V was applied to all three samples for Joule heating. The same size of heating electrodes was used for each condition and the electrode area is indicated with white dot line. (a) 0.8 ml of 0.04 wt% AgNWs was sprayed, followed by 3.0 ml of 0.035 wt% CNTs. **(b)** 1.7 ml of 0.02 wt% AgNWs was sprayed, followed by 2.0 ml of 0.035 wt% CNTs. **(c)** 3.4 ml of 0.01 wt% AgNWs was sprayed, followed by 2.0 ml of 0.035 wt% CNTs. All films showed 1.5 kΩ/sq of sheet resistance.

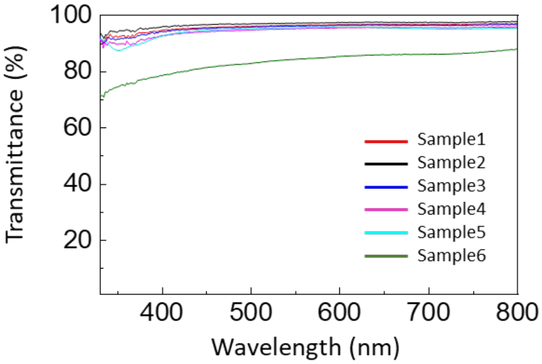

Figure S13. Transmittance spectrum of the hybrid structured electrodes with AgNWs and CNTs (sample 1 – 5) and homogenous CNTs electrode (sample 6). Samples 1 to 5 have increasing amount of CNTs/AgNWs with sheet resistances of 58 kΩ/sq, 28 kΩ/sq, 2 kΩ/sq, 0.7 kΩ/sq, 0.5 kΩ/sq, respectively. The sheet resistance of Sample 6 is 1.5 kΩ/sq.

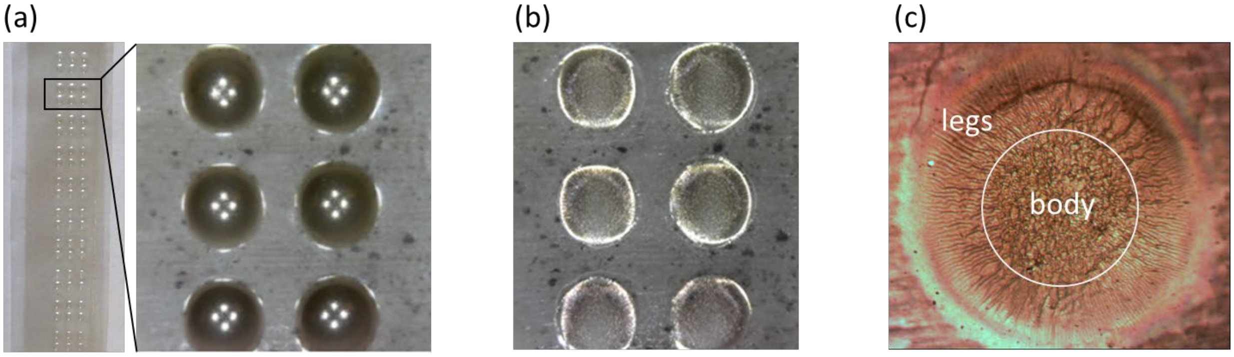

Figure S14. Optical microscopic images of (a) pre-strained state, (b) relaxed (wrinkled) state, and (c) a single dot showing its leg and body areas. The dot diameter is approximately 1.5 mm. Pre-strain ranged from 80 to 100% area strain, correlating with an actuation height of 0.6 to 0.7 mm. In (b) and (c), wrinkled surface scattered more light compared to flat surface in microscopic images.

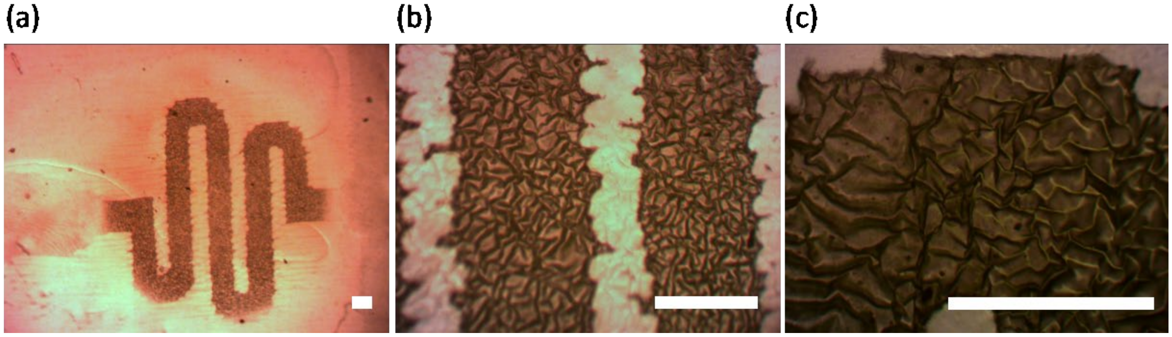

Figure S15. Optical Microscopy images of the wrinkled electrodes after patterning. (a) Entire serpentine-shaped active area, with a boundary between pre-strained and non-pre-strain regions. **(b)** An enlarged centerline, showing a 200 μm width with wrinkles along the line. **(c)** An enlarged image of a serpentine turn. (All scale bars: 200 μm).

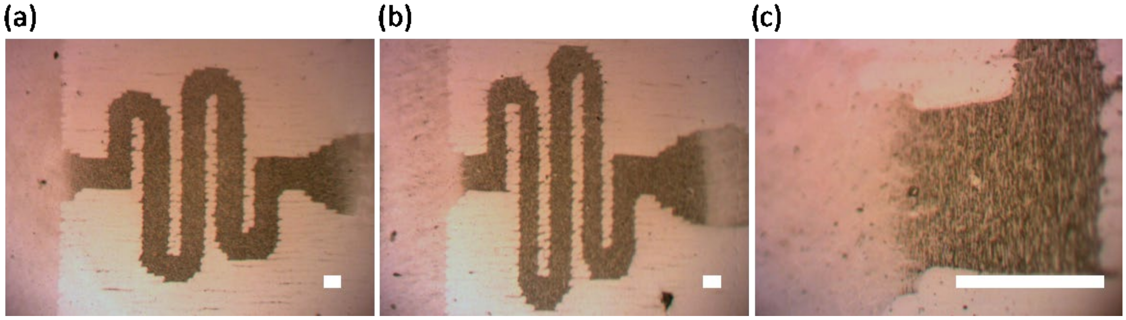

Figure S16. Optical Microscopy images of a uniaxial stretching test. (a) Before stretching, **(b)** after 50% stretching the entire electrode film, and **(c)** an enlarged image (scale bar: 200 μm). The serpentine-patterned electrode underwent uniaxial deformability testing. Prior to stretching, the dark-colored serpentine pattern is the pre-strained area (Figure a). After 50% uniaxial stretching (equivalent to 125% area strain in biaxial), Figure (b) and (c) revealed no micro-cracks across the pattern. The ability of the wrinkles to stretch in the strain direction absorbed the strain energy, preventing cracks initiation and propagation, averting conduction loss. The electrode's relatively low thickness facilitated the unwrinkled bus line to remain free from cracks, unlike the thicker geometry, which exhibited cracking (see Figure S16).

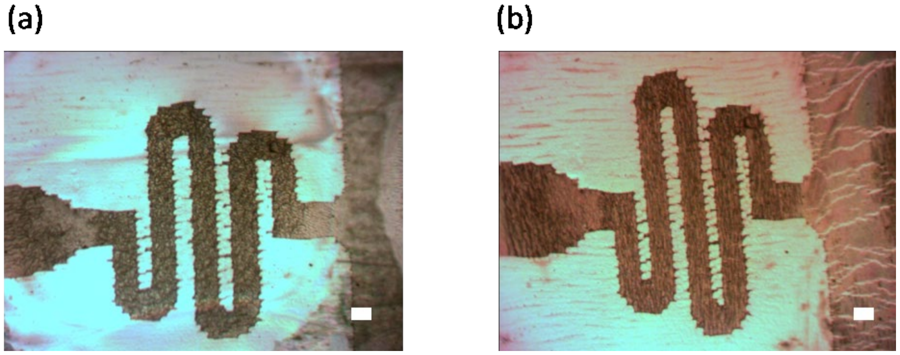

Figure S17. Optical Microscopy images of a uniaxial stretching test of the JHE electrode. **(a)** Before stretching and **(b)** after 30% stretching in the vertical direction (scale bar: 200 μm). Note that only the active area with the serpentine structure has wrinkled structure. After a 30% stretch of the entire electrode film, the bus line area develops multiple cracks.[2-3]

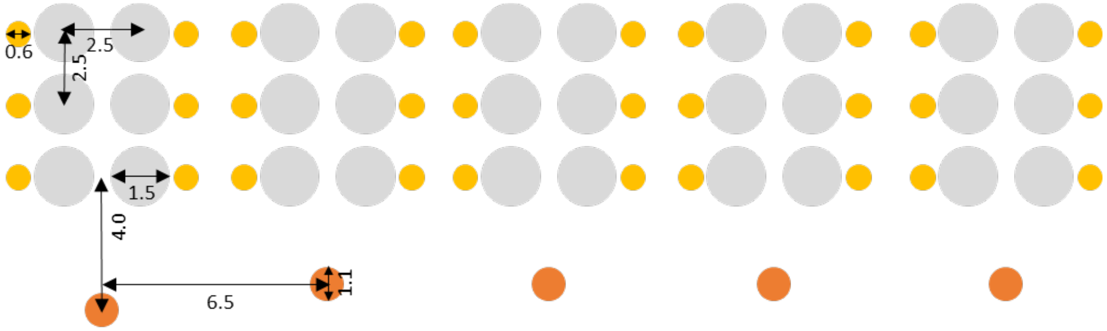

Figure S18. Layout of the PCB for independent control of the dots. Electrical inputs to the dots are supplied via the contacts points marked in gold color. The shared ground is marked in orange. Spacings are in mm.

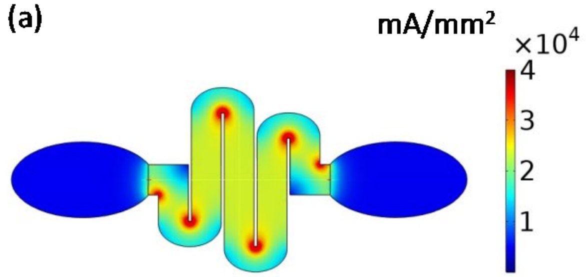

Figure S19. **Finite Element Analysis (FEA) results of current density distribution in (a) serpentine-shaped and (b) spiral-shaped electrodes.** The color bar indicates current density as a Joule heating performance. The conductance between the ground and terminal point is 0.049 S for the serpentine pattern and 0.028 S for the spiral pattern, determined based on the surface area and length. The serpentine pattern has surface area of 1.25 mm^2 and length of 5.34 mm. The spiral pattern has surface area of 1.03 mm^2 and length of 6.42 mm. The serpentine structure displays uniform current flow with around 2.5 X 10^4 mA/mm^2. In contrast, the spiral pattern showed low current density at its circular center around 1.5 X 10^4 mA/mm^2, represented in blue. This results in a 46% difference in resistance, followed by the equation $R = \rho\left(\frac{l}{A}\right)$. The 'extremely fine' mesh was used for accurate steady-state electric conduction, utilizing an isotropic electrical conductivity of SWCNT (10,000 S/m) and a 12V potential difference between the ground and terminal points. The stationary form of the partial differential equation for electric currents: $\nabla \cdot J = Q_{j.v}$, where $J = \sigma E$ (J: current density, σ: conductivity, E: electric field) $E = -\nabla V$ (V: electric potential)

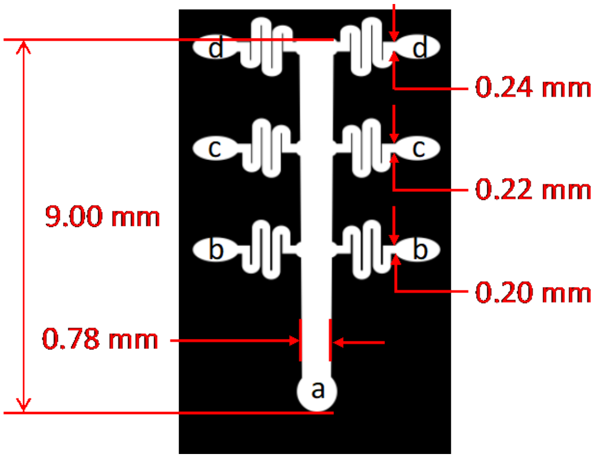

Figure S20. Design of the electrode with a serpentine pattern. Optimized serpentine pattern design for uniform Joule heating and minimized resistance. Point-to-point resistance increases with distance from the bottom contact point on the bus line. The top two contact points have higher resistance than the middle and bottom two contact points. The serpentine pattern width is adjusted to compensate for resistance across all six contact points.

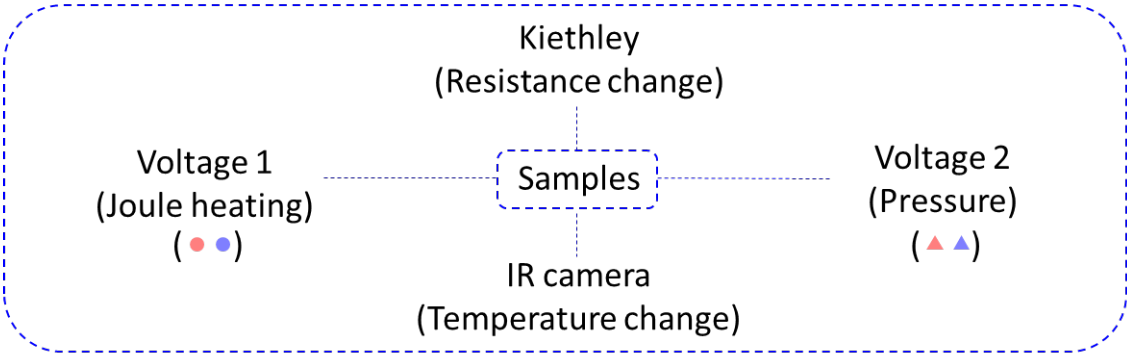

Figure S21. Diagram for the measurement of Joule heating (circles) and actuation (triangles). A set up is designed for resistance and temperature measurement. Using the Keithley and an IR camera, voltage 1 and 2 supply Joule heating and pumping, respectively, following the cycles outlined in Figure S23 (a). The red indicates the “start” points, and the blue indicates the “end” points.

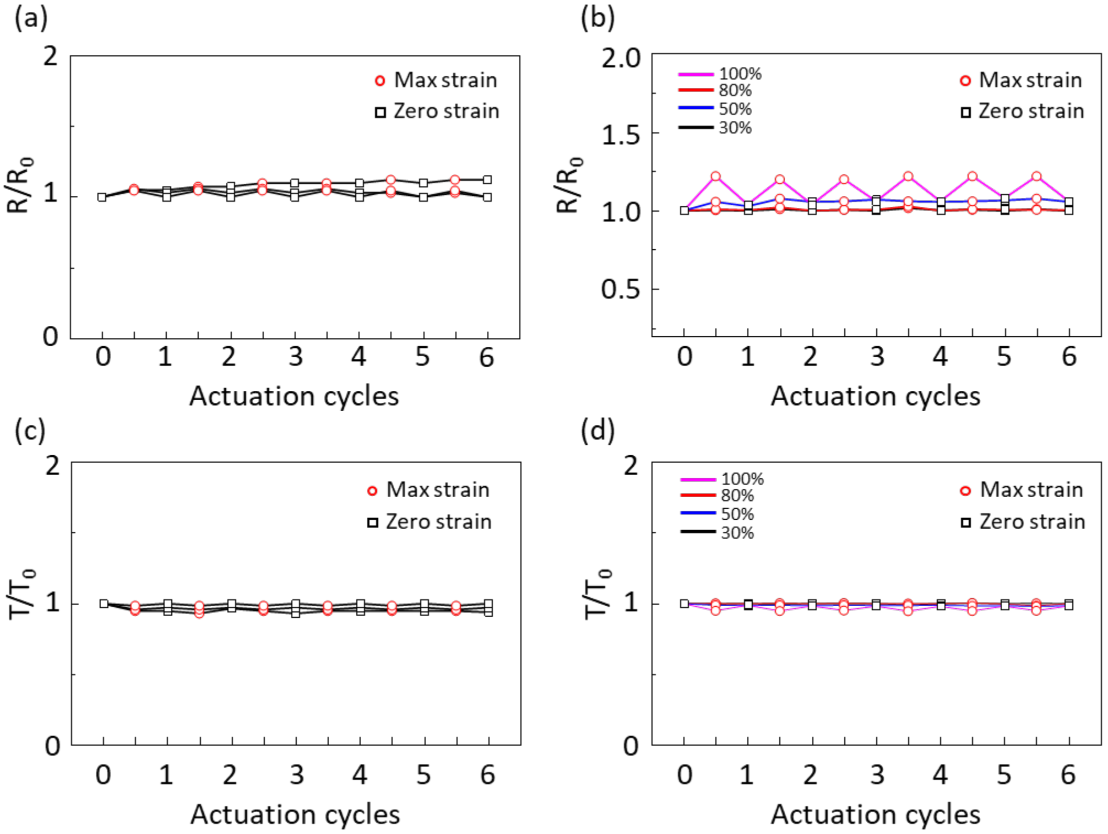

Figure S22. Electromechanical and thermal performance of the Braille system. (a) and (c) show the normalized resistance and temperature change of BSEP membranes with different initial resistances. **(b) and (d)** illustrate the normalized resistance and temperature change of the BSEP membrane under varied actuated area strains from 30% to 100%.

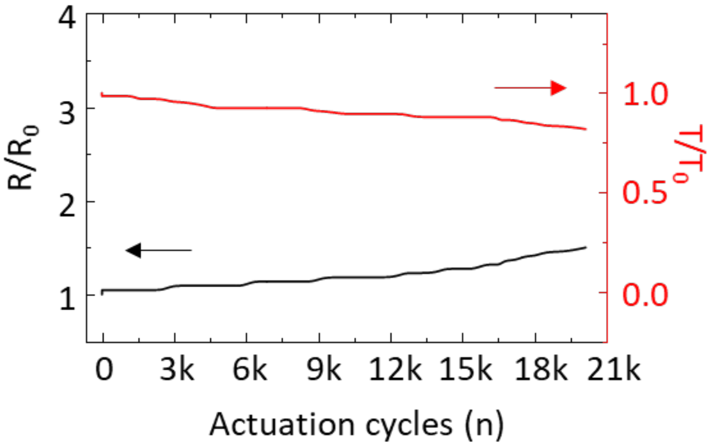

Figure S23. Normalized resistance and temperature in lifetime cyclic test (see Figure 4e for absolute values).

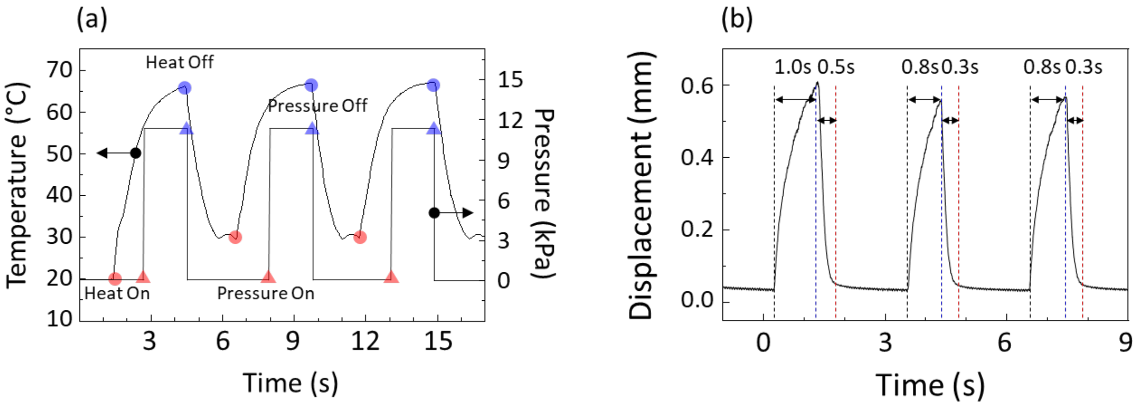

Figure S24. (a) Temperature and pressure profiles during actuation cycles. The circle is for the Joule heating temperature and the triangle is for the pressure. Red color indicates "On" and blue color indicates "Off". Joule heating at 9V for 2-second, followed by applying 8 kPa pneumatic pressure for 2-second to actuate the softened film. A subsequent 2-second relaxation occurs by halting both the Joule heating and pressure input. This cycle was employed for the lifetime cyclic test. **(b)** A pin displacement profile measured by a laser displacement sensor, showing a height range of approximately 0.55 – 0.60 mm. Actuations span 0.8 – 1.0 seconds (between black and blue dash lines), while relaxation spans 0.3 – 0.5 seconds (between blue and red dash lines).

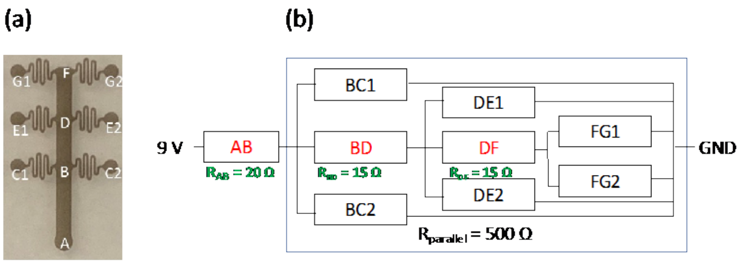

$R_{AC1,\,AC2} = 3.00\ \text{k}\Omega$, $R_{AE1,\,AE2} = 3.04\ \text{k}\Omega$, $R_{AG1,\,AG2} = 3.10\ \text{k}\Omega$

$U_{AB} = 0.38\ \text{V}$, $U_{BD} = 0.19\ \text{V}$, $U_{DF} = 0.10\ \text{V}$

$W_{BC} = U_{bottom}^2/R = (8.62\text{V})^2/\ 2980\Omega = 0.0249\ \text{W}$

$W_{DE} = U_{middle}^2/R = (8.43\text{V})^2/\ 3005\Omega = 0.0236\ \text{W}$

$W_{FG} = U_{top}^2/R = (8.33\text{V})^2/\ 3050\Omega = 0.0227\ \text{W}$

$R_{total} = 520\ \Omega$, $W_{total} = 0.155\ \text{W}$, $W_{heating} = 0.142\ \text{W}$

Figure S25. The calculation for the power consumption and power efficiency for Joule heating on active area of the stretchable electrode. (a) Optical microscopy image for the serpentine patterned electrode and (b) circuitry diagram for its resistance in the electrode. Figure (a) shows the optical image of the patterned electrode with all contact points marked from A to G. To calculate the power consumption and efficiency, the power consumed on each active line and bus line needs to be calculated. As shown in Figure (b), the resistance between point A and the other points is in series. Resistance between each line, top (FG1, FG2), middle (DE1, DE2) and bottom (BC1, BC2) is in parallel. By using the measured values, the resistance between point A and all other points (R_{AC}, R_{AE}, R_{AG}) and resistance on the bus line (R_{AB}, R_{BD}, R_{DF}), the $R_{parallel}$ in Figure (b) is calculated as 0.5 kΩ. With the voltage drop on each line (U_{bottom}, U_{middle}, U_{top}), the power consumed on the active areas is 0.142 W out of 0.155 W of the total power consumption. Hence, the power efficiency for Joule heating on active area is more than 91.6 %. The calculation was based on 9 V of operating voltage.

Table S1. Deformable joule heating electrodes made of polymer nanocomposites and used in a soft actuator system.

Material	Stretchability (%)	Cyclic actuation (#)	Sheet resistance /electrical conductivity	Operating voltage (V)	Unchanged temperature strain (%)	Response time/ remaining time	Application	Ref
WPU/PEDOT:PSS/rGO	530	100	18.2 S cm^{-1}	5	30	NP	thermotherapy	[4]
WPU/Graphene	NP	5 (Bending)	7.5 × 10^{4} Ω/sq	50	NP	<300 s/20min	Body armor	[5]
DWCNT/AgNPs/PET	NP	100 (Bending)	189 Ω/sq	8	NP	30s	NP	[6]
BSEP/S-CNT	188	10K	1 kΩ/sq	30	NP	2s/	Tactile display	[7]
PI/PDMS/AgNW	NP	500 at 4.5 V (Bending)	0.25 Ω/sq	2	Bending strain 4%	30s/3min	Soft actuator	[8]
PDMS/AgNW	30	300	0.5 Ω/sq	25	NP	25s/4 min	Wearable ECG electrodes	[9]
CNT/AgNW/CNT/WPU/BSEP	100	20K	300 Ω/sq	7.7	90% biaxial	1s/5min	Braille multi array display	This work

Method S1. FEA for heating distribution in the serpentine pattern.

The electrical conductivity, thermal conductivity, and density of SWCNT in the model were 10000 S/m, 1000 W/mK, and 1.5 kg/m^3, respectively. A 9V voltage was applied for Joule heating between the ground (6 copper contacts) and the terminal (copper contact on the bus line). Utilizing Joule's first law ($P = I^2R$, where P is the power converted from electrical energy to thermal energy, I is the current, and R is the resistance), heating primarily occurred on the serpentine active area. To improve Joule heating efficiency, a thin layer of Au was deposited on the bus line to maintain low electrical resistance and avoid excessive heating. Also, the width of the top, middle, and bottom serpentine patterns was varied (0.24, 0.22, and 0.20 mm, respectively) to account for resistance difference due to the varying distance between the ground and contact points.

Reference

[1] S. Pillai, J. Wang, Y. Wang, M. Sk, A. Prakoso, C. Park, *Sci. Rep*. **2016**, *6*, 1.
[2] J. Park, W. Hyun, S. Mun, Y. Park, O. O. Park. *ACS Appl. Mater. Interfaces* **2018**, *10*, 7371.
[3] A. Abdelhalim. A. Abdellah, G. Scarpa, P. Lugli. *Carbon* **2013**, *61*, 72.
[4] R. Zhou, P. Li, Z. Fan, D. Du and J. Ouyang, *Journal of Materials Chemistry C*, **2017**, *5*, 1544.
[5] H. Kim, S. Lee and H. Kim, *Sci. Rep.*, **2019**, *9*, 1511.
[6] N. Anusak, J. Virtanen, V. Kangas, V. Promarak and P. Yotprayoonsak, *Thin Solid Films*, **2022**, *750*, 139201.
[7] Y. Qiu, Z. Lu and Q. Pei, *ACS Appl Mater Interfaces*, 2**018,** 10, 24807.
[8] J. C. Shanshan Yao, Zheng Cui and Yong Zhu, *Nanoscale* **2017**, *9*, 3797.
[9] S. Hong, H. Lee, J. Lee, J. Kwon, S. Han, Y. D. Suh, H. Cho, J. Shin, J. Yeo and S. H. Ko, *Adv. Mater*, **2015**, *27*, 4744.